# 6 Double Well Samples

Double, double toil and trouble;
Fire burn and cauldron bubble.

*(William Shakespeare, Macbeth)*

## 6.1 Introduction

Prior research on InAs–GaSb heterostructures in Oxford has considered single InAs wells embedded between GaSb substrate and cap layers [1–4] as well as superlattices consisting of many alternating InAs and GaSb layers [5–8]. For thick GaSb spacers, the behaviour of superlattices follows that of the double heterointerfaces (DHETS). On the other hand, if the GaSb layer thickness is small enough to allow for significant overlap between the electron wave functions centred at different InAs wells, there is a finite dispersion along the growth direction of the superlattice and the energy levels broaden into a series of 'mini-bands' with band widths approximately antiproportional to the layer spacing.

To study the interaction between electron states in different InAs layers more closely, Philip Shields and I prepared a series of samples following the pattern of Fig. 6.1. These samples, which are listed in Table 6.1, contained two InAs wells with thicknesses $t_1 = t_2 = t_w$ separated by a GaSb layer of thickness $t_b$. Both $t_w$ and $t_b$ were varied systematically. The cap thickness $t_{cap}$ of at least 1,500 Å for all samples ensured that effects of the asymmetric band bending caused by the pinning of the Fermi level at the free GaSb surface were minimized. All of these heterostructures were grown in the metal-organic vapour phase epitaxy (MOVPE) reactor in Oxford within a relatively short time under similar conditions. None the less, the

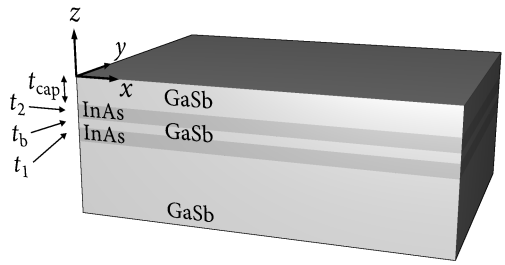


Figure 6.1: Structure of double well samples

| $t_b$/Å | $t_w = 200$ Å | $t_w = 250$ Å | $t_w = 300$ Å |
|---|---|---|---|
| 25 | | OX4538 | |
| 50 | OX4536 | OX4533 | OX4564 |
| 100 | OX4559 | OX4544 | OX4563 |
| 200 | | | OX4574 |
| 300 | | | OX4575 |

Table 6.1: Double well samples by layer dimensions

reproducibility of the epitaxy technique is not perfect and it is only approximately true that the layer thickness was the only parameter that varied between the samples. In particular, there was a measurable difference in surface roughness between different growth runs and between different areas of the same sample.

## 6.2 Calculation of Wave Functions from $\mathbf{k} \cdot \hat{\mathbf{p}}$ Perturbation Theory

### 6.2.1 Principle

The $\mathbf{k} \cdot \hat{\mathbf{p}}$ formalism is an established approximation technique based on second order perturbation theory. It allows the calculation of the energy eigenstates of a solid in a limited region of the momentum space as a linear combination of the eigenstates at a high symmetry point within the region [9,10].

In the presence of a periodic potential $V(\mathbf{r}) = V(\mathbf{r}+\mathbf{R})$, where $\mathbf{R}$ is a lattice vector, the wave function $\varphi(\mathbf{r})$ of an electron obeys the time-independent Schrödinger equation

$$\left[\frac{\hat{\mathbf{p}}^2}{2m_\mathrm{e}} + V(\mathbf{r})\right]\varphi(\mathbf{r}) = E\varphi(\mathbf{r}) \tag{6.1}$$

with $\hat{\mathbf{p}} = -i\hbar\,\nabla_{\mathbf{r}}$. Using the Bloch theorem, $\varphi_{n\mathbf{k}}(\mathbf{r}) = u_{n\mathbf{k}}(\mathbf{r})\exp(i\mathbf{k}\cdot\mathbf{r})$, where $\mathbf{k}$ is the crystal momentum, Eq. (6.1) can be expressed in terms of the Bloch functions $u_{n\mathbf{k}}(\mathbf{r}) = u_{n\mathbf{k}}(\mathbf{r}+\mathbf{R})$ as

$$\left[\frac{\hat{\mathbf{p}}^2}{2m_\mathrm{e}} + \frac{\hbar}{m_\mathrm{e}}\mathbf{k}\cdot\hat{\mathbf{p}} + \frac{\hbar^2\mathbf{k}^2}{2m_\mathrm{e}} + V(\mathbf{r})\right]u_{n\mathbf{k}}(\mathbf{r}) = E_n(\mathbf{k})u_{n\mathbf{k}}(\mathbf{r}). \tag{6.2}$$

The eponymous $\mathbf{k}\cdot\hat{\mathbf{p}}$ term is then treated as a perturbation to the Hamiltonian at $\mathbf{k}_0 = \mathbf{o}$, and to lowest non-vanishing order in $|\mathbf{k}|$, the approximated Bloch wave functions and energies become

$$|u_{n\mathbf{k}}\rangle = |u_{n\mathbf{0}}\rangle + \sum_{m\neq n}\frac{\langle u_{n\mathbf{0}}|\mathbf{k}\cdot\hat{\mathbf{p}}|u_{m\mathbf{0}}\rangle}{E_n(\mathbf{o}) - E_m(\mathbf{o})}|u_{m\mathbf{0}}\rangle \qquad \text{and} \tag{6.3}$$

$$E_n(\mathbf{k}) = E_n(\mathbf{o}) + \frac{\hbar^2\mathbf{k}^2}{2m_\mathrm{e}} + \frac{\hbar^2}{m_\mathrm{e}^2}\sum_{m\neq n}\frac{\left|\langle u_{n\mathbf{0}}|\mathbf{k}\cdot\hat{\mathbf{p}}|u_{m\mathbf{0}}\rangle\right|^2}{E_n(\mathbf{o}) - E_m(\mathbf{o})}. \tag{6.4}$$

The choice $\mathbf{k}_0 = \mathbf{o}$ is appropriate for III–V materials because the extrema of both the valence and the conduction bands lie at the Γ-point (*cf.* Fig. 5.2(a)), but the method can be generalized straightforwardly to other $\mathbf{k}_0$.

### 6.2.2 Application to InAs–GaSb Heterostructures in a Magnetic Field

I used a programme originally developed at Oxford by Thomas Vaughan for calculating the band structure of infinite GaSb–InAs superlattices close to the Γ-point. The software has successfully been used to predict a wide range of experimental superlattice results [5, 11] and has also been applied to single-well systems by increasing the distance between InAs layers to the extent that the overlap of wave functions at different wells becomes negligible or by introducing virtual large bandgap spacer layers [4, 12]. As the implementation details are discussed extensively in Vaughan's thesis [11] and the references therein, I shall restrict myself to summarizing the crucial points of the computation.

A realistic calculation of the energy levels at high symmetry points in III–V semiconductors entails taking spin–orbit coupling into account. This leads to an additional term of the form $\hbar/(2m_e c)^2 \left[\nabla_{\mathbf{r}} V(\mathbf{r}) \times \hat{\mathbf{p}}\right] \cdot \boldsymbol{\sigma}$ in Eq. (6.1), where $\boldsymbol{\sigma}$ is a vector containing the Pauli spin matrices as elements. If an external magnetic field is present, $\hat{\mathbf{p}}$ becomes $\hat{\mathbf{p}} + e\mathbf{A}(\mathbf{r})$, where $\mathbf{A}(\mathbf{r})$ is the magnetic vector potential, and there is a further electron spin contribution $\frac{1}{2} g \mu_B \mathbf{B} \cdot \boldsymbol{\sigma}$ to the Hamiltonian, where $g \approx 2$ is the Landé $g$-factor and $\mathbf{B}$ is the magnetic flux density.[1] The spin–orbit and spin splitting terms can be treated perturbatively. If the coordinate system is chosen with one axis along the direction of the magnetic field, the Schrödinger equation becomes separable as outlined in Sec. 5.6.2.

Instead of expressing the wave function in the infinite basis formed by the Bloch waves at $\mathbf{k} = \mathbf{0}$, Löwdin's orthogonalization method [13] was used with a limited set of eight basis states. Following Kane [14], the basis states were chosen as linear combinations of atomic orbitals that corresponded to the conduction band, the light and heavy hole bands, and the split-off (spin-orbit) hole band (with two spin states each).

To account for the effect of the heterojunctions, the expansion coefficients in the chosen basis were allowed to vary as a function of position, so that the wave function was effectively a superposition of atomic orbitals modulated by an envelope function; it was implicitly assumed that the basis states are the same for both materials. These simplifications, known as the envelope function approximation (EFA), are valid for most material systems as long as the envelope function varies slowly on the scale of the interatomic distance [11]. The envelope function was calculated in momentum space using an approach analogous to the transfer matrix technique. As explained in Sec 5.5.2, the negative band offset causes a net charge transfer from the GaSb layers to the InAs layers if the InAs wells are sufficiently wide. The programme performed several iterations until it arrived at an effective potential that was consistent with the calculated envelope functions. In a heterostructure, the simple treatment of the magnetic field was restricted to field directions parallel to the growth direction (and, at the same time, parallel to a direction of high symmetry of the crystal lattice).

[1] This is the term that leads to Zeeman splitting of the energy levels.

### 6.2.3 Double Well Calculations

Modelling DHETs and double well samples using this approach poses additional challenges. A virtual superlattice[2] must be constructed in such a way that the interaction between different periods is effectively minimized. This can be achieved by inserting either sufficiently thick bulk-like GaSb layers or additional layers of a large bandgap material such as AlSb. The addition of such fictitious layers introduces further parameters that can be adjusted to match experimental data and has successfully been used to predict Landau level diagrams of thin cap (asymmetric) DHETs that are in good agreement with observation [4, 12]. In double well samples, however, such an additional layer would either reduce the interaction between the layers or introduce a strong asymmetry between them.

The heterostructures were represented by a symmetrical model in these preliminary calculations. In real samples, this symmetry is broken by trapped charges at either the sample surface or the heterojunctions. In the structures discussed here, there was a thick GaSb cap layer and the effect of surface states could be assumed to be small.[3] The charge and the band offset at the interfaces depend on the growth conditions; previous studies have shown that the band offset is larger for InSb-like interfaces than for GaAs-like ones [12]. In our case, the interfaces were nominally unbiased; none the less the possibility of an imbalance between GaSb–InAs and InAs–GaSb interfaces could not be excluded.

For thick layers, the calculation systematically underestimated the confinement energies of both electrons and holes. Whereas experimental data has consistently shown no occupation of subbands other than the ground subband [4] for InAs wells as thick as 340 Å, the $\mathbf{k}\cdot\hat{\mathbf{p}}$ calculation for a symmetric DHET predicted occupation of the second subband at around 200 Å; a similar issue was encountered for holes in thick bulk-like GaSb layers. I calculated energy spectra for double well structures with different barrier thicknesses $t_b$ using the $\mathbf{k}\cdot\hat{\mathbf{p}}$ method. One such calculation is shown in Fig. 6.2 for an InAs well thickness $t_w = 180$ Å; this is smaller than the well thickness in any of the experimental samples but correctly rep-

[2] Which is essential for the momentum matrix technique [11].
[3] See also the discussion in Chapter 7.

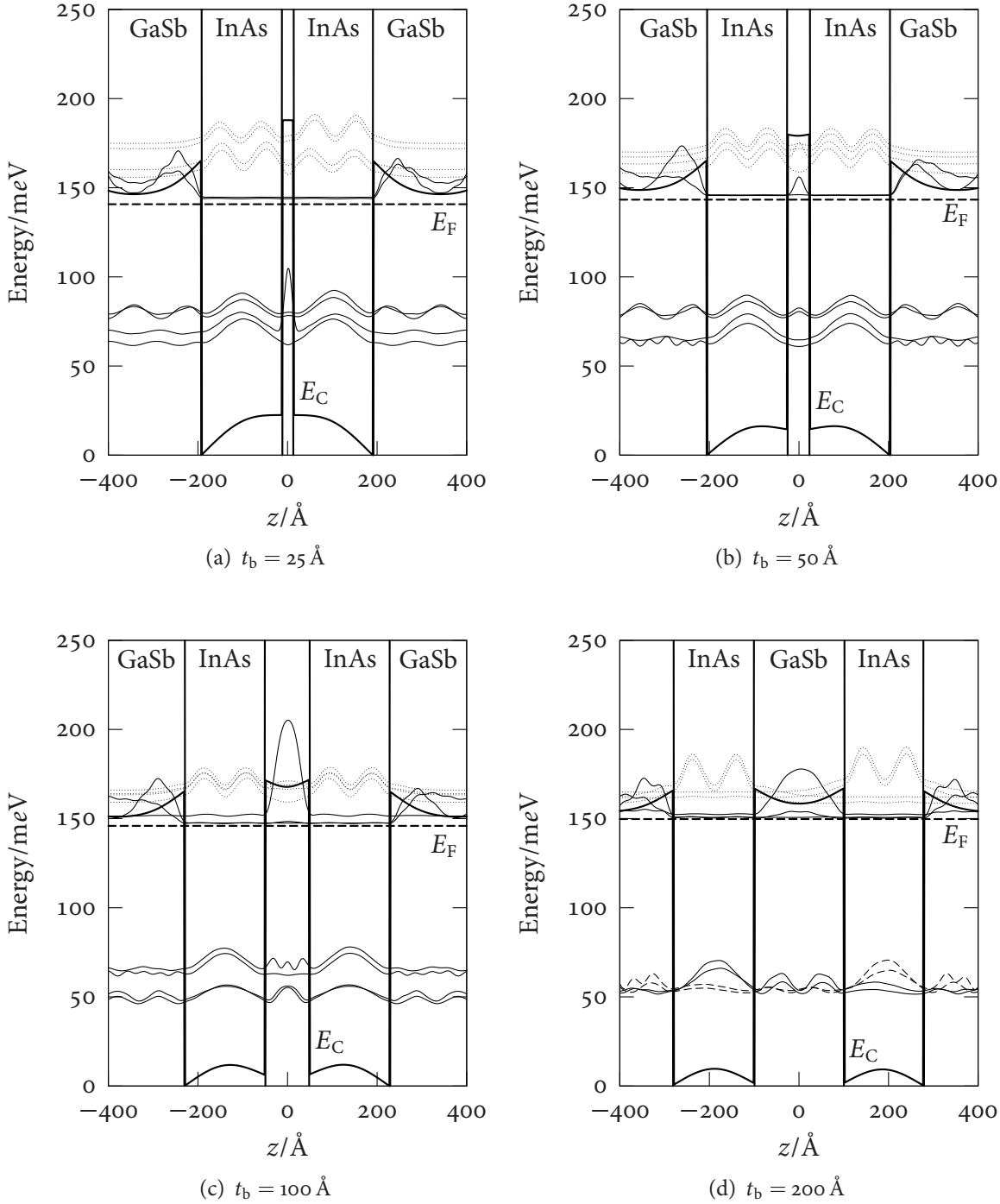


(a) $t_b = 25$ Å (b) $t_b = 50$ Å

(c) $t_b = 100$ Å (d) $t_b = 200$ Å

Figure 6.2: Electron and hole states in double well structures, calculated for a conduction band offset of 140 m$e$V, $t_w = 180$ Å, and $B_z = 1$ T. For conduction band states below and valence band states above the Fermi level, the probability densities are shown in arbitrary units, vertically offset by the energy of the state. Dotted lines represent the unoccupied second electron subband.

resents the situation in which only one electron subband is occupied. For small barrier thicknesses, the InAs conduction band states in the two wells mixed. On increasing the barrier width from 50 to 100 Å, hole levels appeared in the barrier, which approached those in the bulk GaSb on either side of the double well structures if the barrier was made even wider. Increased localization of conduction band states to either InAs well was predicted for large $t_b$.

## 6.3 Experimental Results

### 6.3.1 Overview of Individual Samples

To perform magnetotransport measurements on the double well samples, I created a number of Hall bars with a width of 20 µm and an aspect ratio of 2 : 1 by means of optical lithography. I then measured the sheet resistivity components in magnetic fields up to 18 T both in a perpendicular field configuration with $B = B_z$ pointing in the growth direction and in a parallel field configuration with $B = B_\parallel$ lying in the plane of the carriers along the $\langle 100 \rangle$ family of crystallographic directions, either parallel or perpendicular to the excitation current $I_x(t)$. All data were taken at 0·5, 1·5, or 4·2 K according to the procedures laid down in Chapter 4.

Table 6.2 shows an overview of these measurements and displays a number of overall sample properties. Estimates of the sheet carrier concentration were obtained from the frequency of the low field Shubnikov-de Haas-oscillations ($n_{\mathrm{SdH}}$) as well as the Hall coefficient around $B_z = 0$ ($n_{R_\mathrm{H}}$); in all samples the latter value was significantly higher than the the former, with ratios $n_{R_\mathrm{H}} : n_{\mathrm{SdH}} > 2$ for samples with large barrier thicknesses $t_b$. Almost all samples showed a very strong negative magnetoresistance in a parallel field $B_\parallel$. The resistivity typically saturated for $B_\parallel > 12\,\mathrm{T}$; for many samples, $\rho_{\mu\mu}$ dropped to less than a fourth of its zero field value.

Fitting the low field ($B_z < 2\,\mathrm{T}$) data for the large $t_b$ sample 0X4575 to the semiclassical Drude model of Sec. 5.6.1 indicated similar electron and hole concentrations, but did not

(a) $t_w = 200$ Å

| $t_b$ (Å) | Sample | $T$ (K) | $n_{SdH}$ ($10^{11}$/cm$^2$) | $n_{R_H}$ ($10^{11}$/cm$^2$) | $\frac{n_{R_H}}{n_{SdH}}$ | $\frac{\rho_{\mu\mu}(0)}{\rho_{\mu\mu}^{(min)}(B_\parallel)}$ | $\frac{\rho_{\mu\mu}^{(max)}(B_\parallel)}{\rho_{\mu\mu}^{(min)}(B_\parallel)}$ |
|---|---|---|---|---|---|---|---|
| 50 | A | 4·2 | 6·2 | 10·6 | 1·7 | 3·4 | 4·6 |
| | B | 0·5 | 5·9 | 12·0 | 2·0 | 2·5 | 3·3 |
| | C | 0·5 | 6·4 | 10·5 | 1·6 | 4·5 | 4·7 |
| 100 | A | 4·2 | 6·0 | 9·8 | 1·6 | 1·6 | 1·9 |
| | B | 0·5 | 6·1 | 9·2 | 1·5 | | |

(b) $t_w = 250$ Å

| $t_b$ (Å) | Sample | $T$ (K) | $n_{SdH}$ ($10^{11}$/cm$^2$) | $n_{R_H}$ ($10^{11}$/cm$^2$) | $\frac{n_{R_H}}{n_{SdH}}$ | $\frac{\rho_{\mu\mu}(0)}{\rho_{\mu\mu}^{(min)}(B_\parallel)}$ | $\frac{\rho_{\mu\mu}^{(max)}(B_\parallel)}{\rho_{\mu\mu}^{(min)}(B_\parallel)}$ |
|---|---|---|---|---|---|---|---|
| 25 | A | 4·2 | 6·0 | 9·4 | 1·6 | | |
| | B | 4·2 | 6·1 | 8·7 | 1·4 | 1·3 | 1·6 |
| | B | 1·5 | 6·9 | 8·8 | 1·3 | 1·3 | 1·6 |
| | C | 0·5 | 6·2 | 9·4 | 1·5 | 3·6 | 4·5 |
| 50 | A | 4·2 | 6·7 | 9·8 | 1·5 | 1·1 | 1·8 |
| | B | 0·5 | 7·0 | 12·3 | 1·8 | 4·0 | 5·6 |
| 100 | A | 4·2 | 7·0 | 17·8 | 2·8 | 3·6 | 6·2 |
| | B | 0·5 | 7·6 | 18·4 | 2·4 | 5·5 | 7·1 |

(c) $t_w = 300$ Å

| $t_b$ (Å) | Sample | $T$ (K) | $n_{SdH}$ ($10^{11}$/cm$^2$) | $n_{R_H}$ ($10^{11}$/cm$^2$) | $\frac{n_{R_H}}{n_{SdH}}$ | $\frac{\rho_{\mu\mu}(0)}{\rho_{\mu\mu}^{(min)}(B_\parallel)}$ | $\frac{\rho_{\mu\mu}^{(max)}(B_\parallel)}{\rho_{\mu\mu}^{(min)}(B_\parallel)}$ |
|---|---|---|---|---|---|---|---|
| 50 | A | 4·2 | 6·9 | 11·4 | 1·7 | 5·1 | 5·5 |
| | B | 4·2 | 7·5 | 11·5 | 1·5 | 1·5 | 2·0 |
| | B | 1·5 | 7·0 | 10·7 | 1·5 | 1·6 | 2·1 |
| 100 | A | 4·2 | 7·3 | 15·9 | 2·2 | 4·3 | 8·3 |
| | B | 0·5 | 7·7 | 16·9 | 2·2 | 3·2 | 4·3 |
| | C | 0·5 | 7·6 | 15·9 | 2·1 | 4·0 | 6·2 |
| 200 | A | 4·2 | 6·9 | 16·0 | 2·3 | 3·9 | 4·1 |
| | B | 0·5 | 7·4 | 16·3 | 2·2 | 3·7 | 3·9 |
| | C | 0·5 | 7·3 | 16·4 | 2·2 | 3·7 | 4·1 |
| 300 | A | 4·2 | 6·5 | 16·2 | 2·5 | 2·6 | 3·8 |
| | B | 0·5 | 7·4 | 16·6 | 2·2 | 3·1 | 3·2 |
| | C | 0·5 | 7·4 | 16·3 | 2·2 | 3·1 | 3·2 |

Table 6.2: Overview of individual samples. The concentrations $n_{SdH}$ and $n_{R_H}$ were calculated from the frequency of the Shubnikov-de Haas-oscillations in a low (0·4 to 1·2 T) field and from the Hall coefficient $R_H(0)$ around the origin ($B_z < 0{\cdot}5$ T).

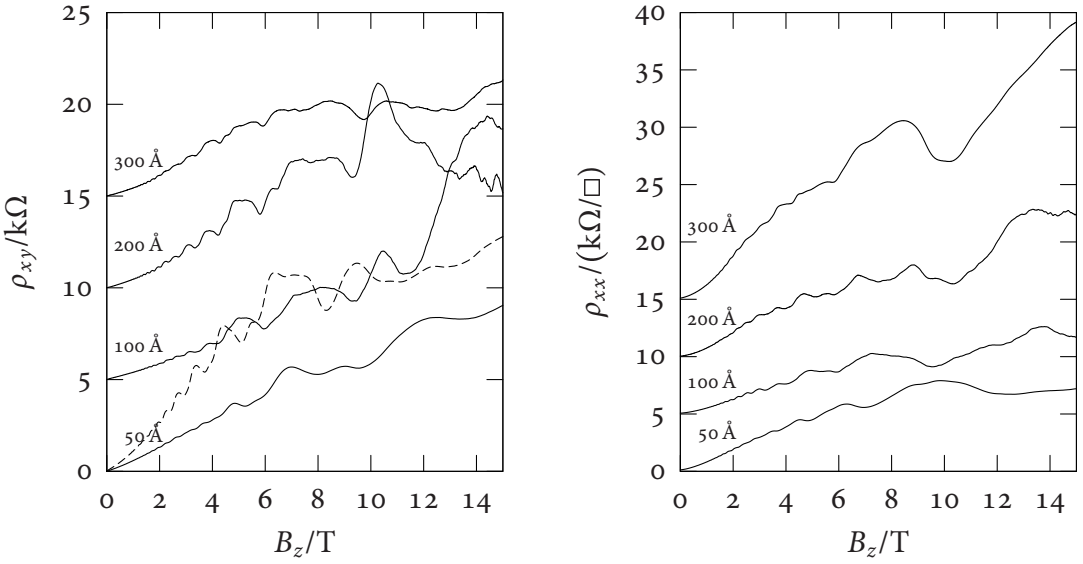


(a) Hall resistivity (b) Magnetoresistivity

Figure 6.3: Hall resistivity and magnetoresistivity of $t_w = 300\,\text{nm}$ samples for $t_b = 50\,\text{Å}$ (bottom), 100 Å, 200 Å, and 300 Å (top). Individual curves are offset by 5 kΩ for clarity. All samples were measured at $T = 0{\cdot}5\,\text{K}$, except 0x4564 ($t_b = 50\,\text{Å}$), for which $T = 1{\cdot}5\,\text{K}$. The dashed line in (a) represents the $t_w = 300\,\text{Å}$ DHET 0x4576.

yield stable estimates for the absolute concentrations and mobilities. The resistivity is dominated by the minigap formed as a result of electron–hole hybridization (*cf.* Sec 5.5.3). Using the magnetoresistance at large $B_\parallel > 12\,\text{T}$ together with $n_e = 2n_{SdH}$ to remove the effect of the minigap, an electron mobility of 130,000 $\text{cm}^2/(\text{Vs})$ for 0x4575 and 230,000 $\text{cm}^2/(\text{Vs})$ for 0x4574 was estimated.

### 6.3.2 Magnetoresistance Data

#### Perpendicular Magnetic Field

For large barrier thicknesses $t_b > 100\,\text{Å}$, the behaviour of the magnetoresistivity did not depend strongly on $t_b$. This is illustrated in Fig. 6.3, which contrasts samples with different $t_b$ but identical well width $t_w = 300\,\text{Å}$. The intermediate magnetic field features were similar for samples with $t_b = 100\,\text{Å}$, 200 Å, and 300 Å and occurred at similar field values. While

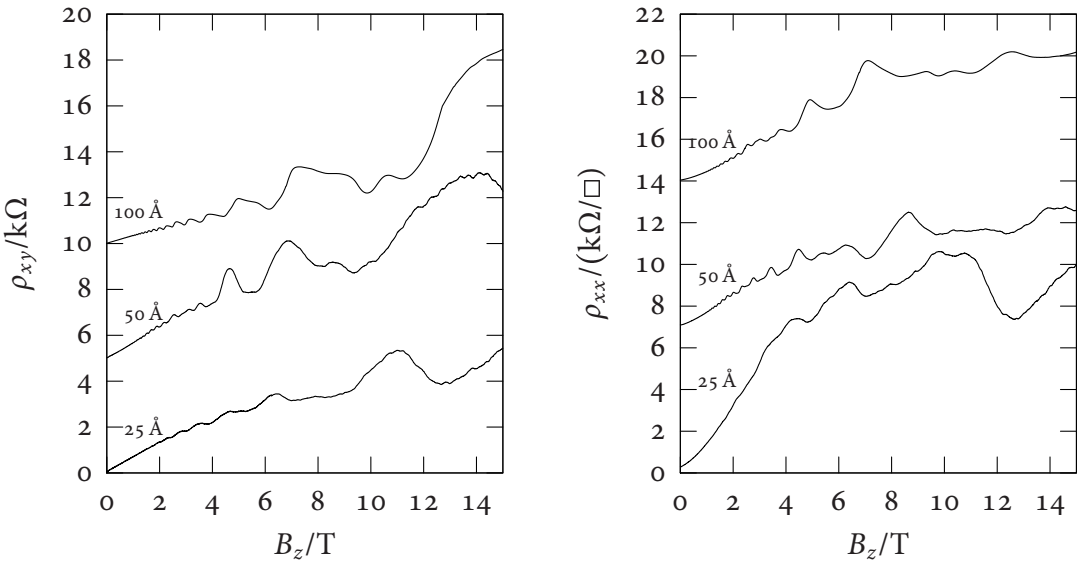


(a) Hall resistivity (b) Magnetoresistivity

Figure 6.4: Hall resistivity and magnetoresistivity of $t_w = 250$ nm samples for $t_b = 25$ Å (bottom), 50 Å, and 100 Å (top). Individual curves are offset by 5 kΩ in (a) and 7 kΩ in (b). All samples were measured at $T = 0{\cdot}5$ K, except 0x4544 ($t_b = 100$ Å), for which $T = 4{\cdot}2$ K.

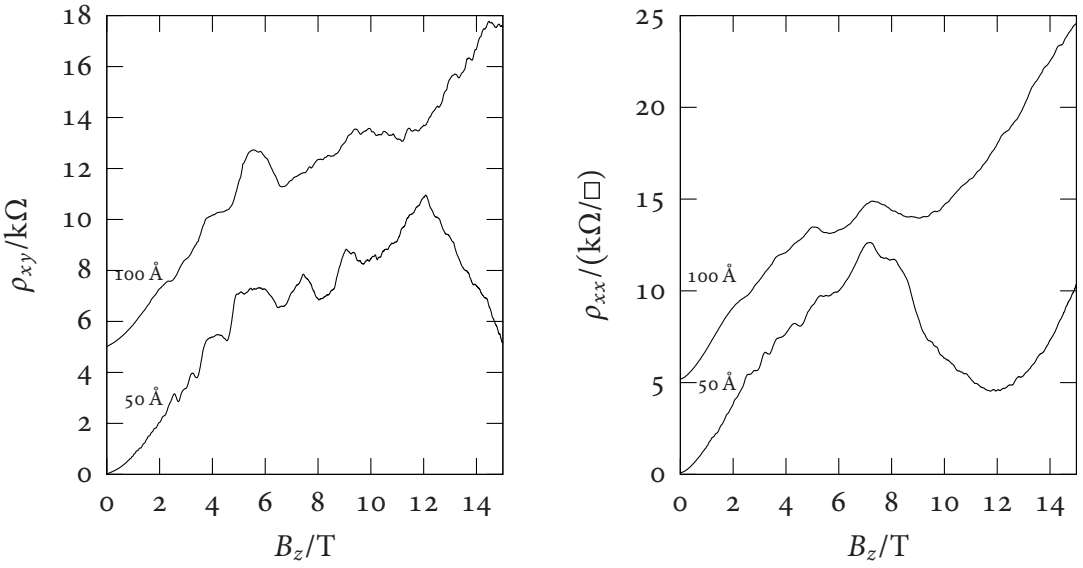


(a) Hall resistivity (b) Magnetoresistivity

Figure 6.5: Hall resistivity and magnetoresistivity of $t_w = 200$ nm samples for $t_b = 50$ Å (bottom) and 100 Å (top). Individual curves are offset by 5 kΩ for clarity. Both samples were measured at $T = 0{\cdot}5$ K.

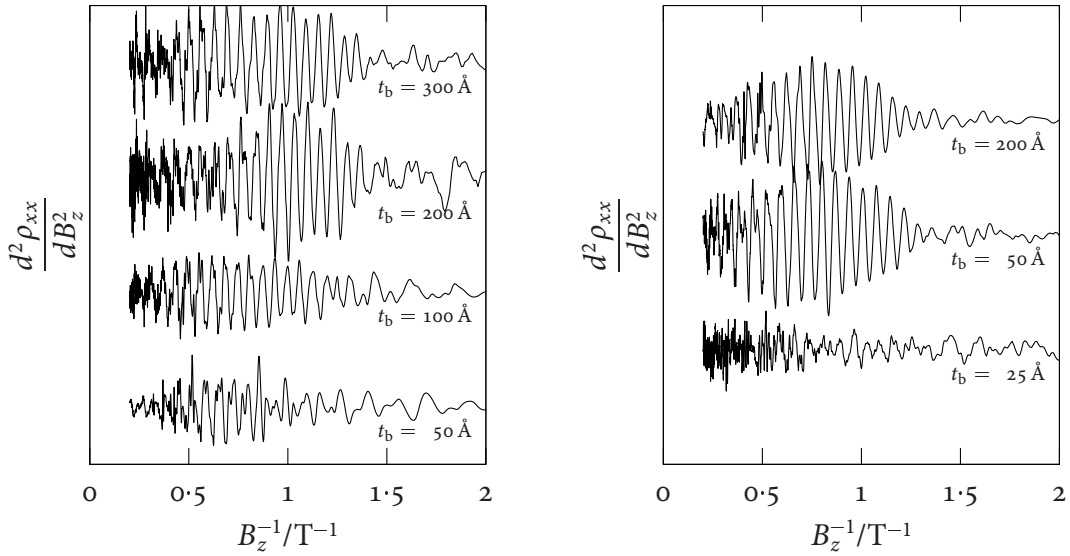


(a) $t_w = 300$ Å (b) $t_w = 250$ Å

Figure 6.6: Shubnikov–de Haas-oscillations in double well samples. The second derivative of $\rho_{xx}(B_z)$ taken from Figs. 6.3 and 6.4 is plotted against $1/B_z$. Individual curves are offset for clarity.

there are still noticeable differences between these curves, they are not significant in the sense that different pieces of the same sample showed similar disparities. Compared to the Hall resistivity of the single DHET 0X4576 with $t_w = 300$ Å and $t_{cap} = 1{,}500$ Å, overlaid on Fig. 6.3(a), the double well samples exhibited analogous features shifted to (approximately 10 %) higher field. The magnitude of $\rho_{xy}$ was halved.

On decreasing the barrier thickness further from 100 Å, the situation became more complicated, as may be seen from the $t_b = 50$ Å trace in Fig. 6.3 and also from Figs. 6.4 and 6.5, which show similar comparisons for samples with $t_w = 250$ Å and 200 Å. The magnetoresistivity features changed qualitatively and could no longer straightforwardly be connected to comparable features observed for samples with larger $t_b$.

Fig. 6.6 shows the second derivative of $\rho_{xx}(B_z)$ plotted against $1/B_z$ and allows a closer look at the Shubnikov–de Haas-oscillations in these samples. The oscillations exhibited a

single dominating frequency. Splitting of individual peaks was seen in some traces, and a single sample ($t_w = 300$ Å, $t_b = 50$ Å) showed indications of a distinct second oscillation frequency, corresponding to $n_{SdH} = 3{\cdot}2 \pm 0{\cdot}2\,\mathrm{cm}^{-2}$. However, there was no compelling evidence for the beating pattern that would be associated with two incommensurate oscillation frequencies with comparable values.

### Parallel Field

There was considerable variation in the parallel field longitudinal resistivity $\rho_{\mu\mu}(B_\parallel)$ of the double well samples, shown in Fig. 6.7 for an excitation current parallel to the in-plane field. For all of these samples, $\rho_{xx}(B_\parallel)$ reached a maximum at a low field ($B_\parallel < 4$ T). A further pronounced feature occurred around 10 T. The magnetoresistance either exhibited a shoulder and dropped to a saturation value for $B_\parallel > 12$ T or it reached a second maximum—which could exceed the low field one—and continued to decrease over the investigated field region. The magnetoresistance in the direction perpendicular to the current, $\rho_{yy}(B_\parallel)$, showed similar behaviour in the limit of low and high fields and less pronounced maxima (not shown); direct comparison is problematic as these data were taken on different areas of the samples.

The thick barrier samples with $t_b = 200$ Å or 300 Å and $t_w = 300$ Å behaved consistently and always had a maximum at or close to $B_\parallel = 0$ T and a saturated resistance of a quarter to a third of the zero field value at high parallel fields.

### Quantum Well Width

The comparison of the perpendicular field magnetoresistance traces for different well thicknesses $t_w$ in Fig. 6.8 showed similar structure, which was shifted to lower magnetic field values for larger well widths. No clear trend emerged in the parallel field traces, which are collated in Fig. 6.7. In so far as features were directly comparable, they were shifted to higher fields for samples with thinner InAs wells.

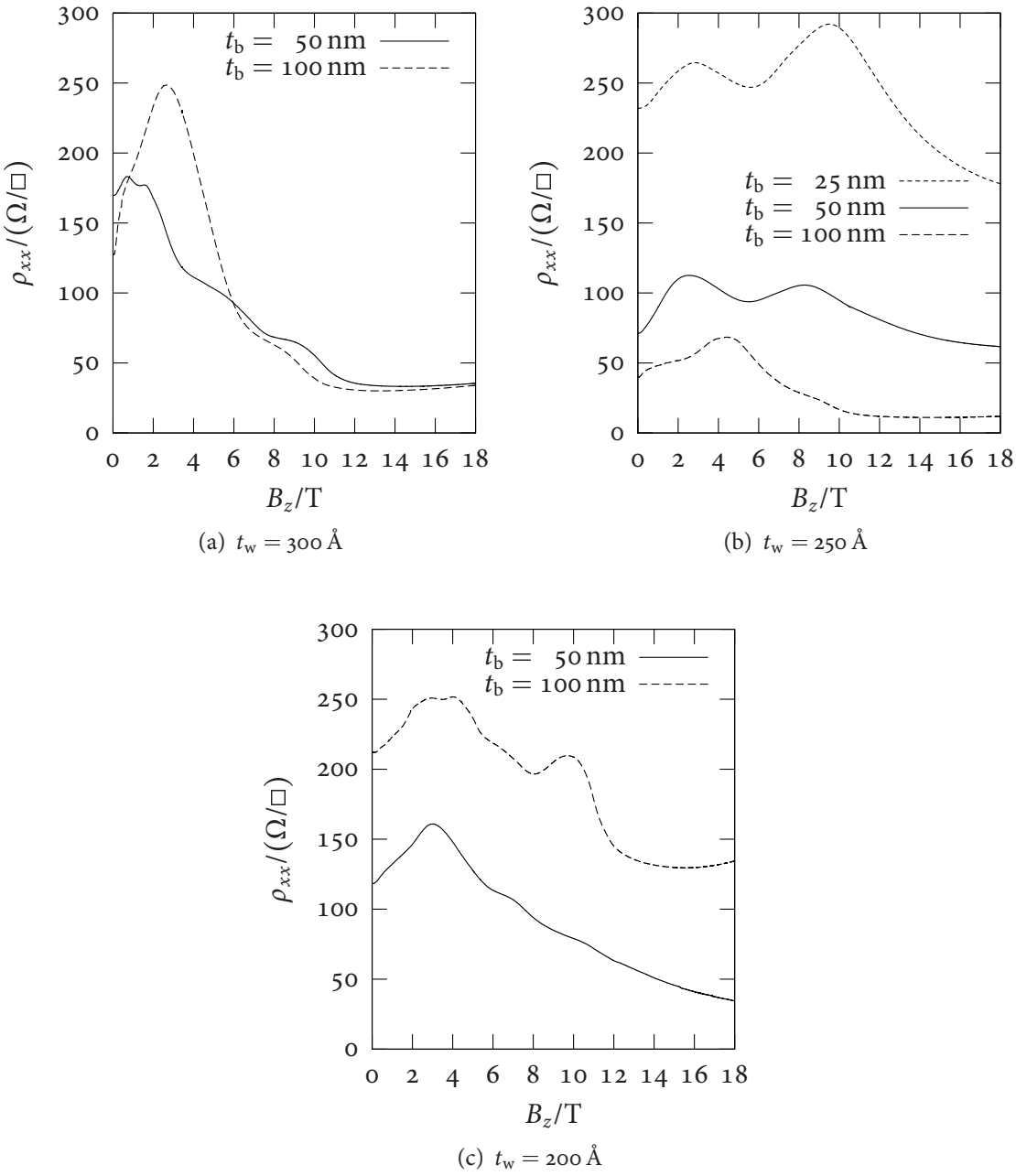


(a) $t_w = 300\,Å$

(b) $t_w = 250\,Å$

(c) $t_w = 200\,Å$

Figure 6.7: Parallel field magnetoresistance of double well samples, measured with the magnetic field parallel to the excitation current. All samples were measured at $T = 4{\cdot}2\,K$.

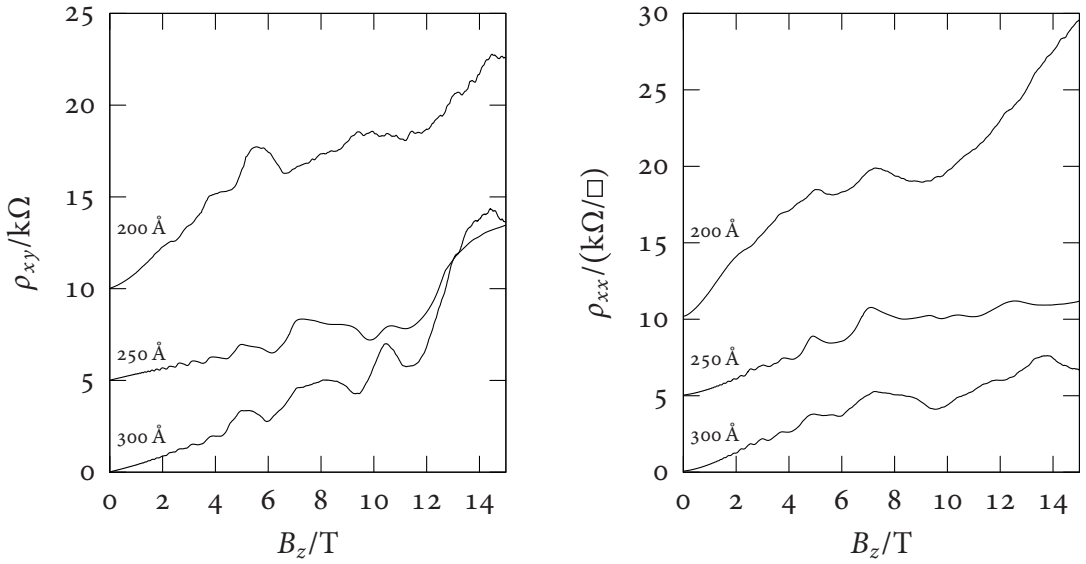


(a) Hall resistivity (b) Magnetoresistivity

Figure 6.8: Hall resistivity and magnetoresistivity of $t_b = 100$ nm samples for $t_w = 300$ Å (bottom), 250 Å and 200 Å (top). Individual curves are offset by 5 kΩ in (a) and 7 kΩ in (b). All samples were measured at $T = 0{\cdot}5$ K, except 0x4544 ($t_b = 100$ Å), for which $T = 4{\cdot}2$ K.

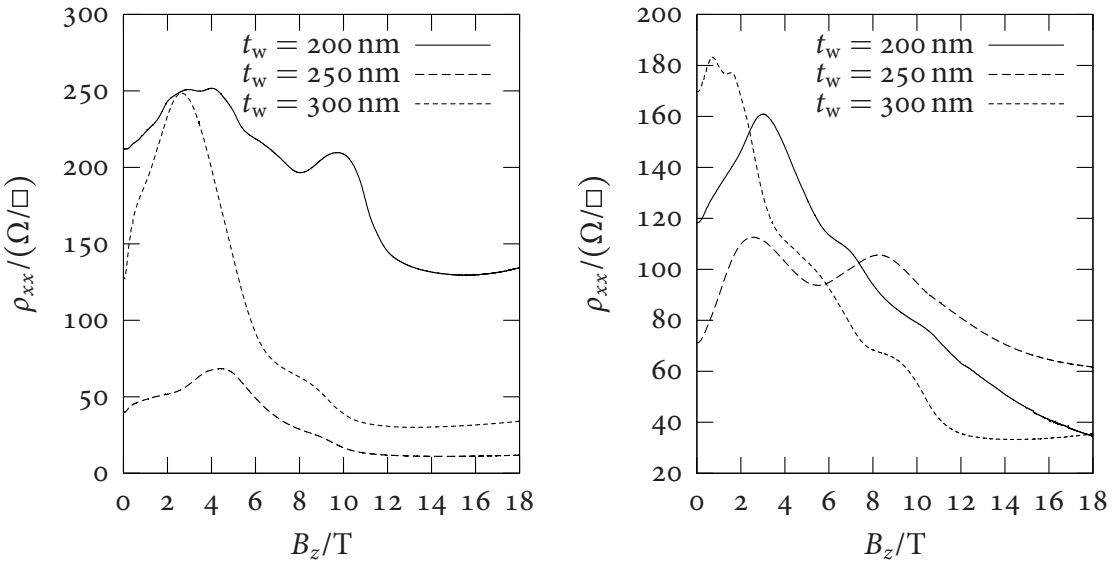


(a) $t_b = 100$ Å (b) $t_b = 50$ Å

Figure 6.9: Parallel field magnetoresistance of samples with different well widths, measured with the magnetic field parallel to the excitation current. All samples were measured at $T = 4{\cdot}2$ K.

## 6.4 Discussion

### 6.4.1 Carrier Concentration

In the limit of small magnetic fields, the semiclassical expression for the Hall resistance of a two dimensional gas of electrons and holes, Eq. (5.25), simplifies to

$$\rho_{xy} \approx \frac{B_z}{e} \frac{n_\mathrm{e}\mu_\mathrm{e}^2 - n_\mathrm{h}\mu_\mathrm{h}^2}{(n_\mathrm{e}\mu_\mathrm{e} + n_\mathrm{h}\mu_\mathrm{h})^2}. \tag{6.5}$$

The Hall coefficient, $R_\mathrm{H} = -\rho_{xy}/B_z$, is therefore dominated by the highest mobility carrier species and the slope of $\rho_{xy}(B_z)$ close to $B_z = 0\,\mathrm{T}$ can be used to estimate the *total* density $n_{R_\mathrm{H}}$ of electrons participating in charge transport. On the other hand, the concentration $n_\mathrm{SdH}$ estimated from the low field Shubnikov–de Haas-oscillations using Eq. (5.32) depends ultimately on the assumed Landau level degeneracy of Eq. (5.30). The observation that $n_{R_\mathrm{H}} \approx 2n_\mathrm{SdH}$ for all samples with barrier thicknesses $t_\mathrm{b}$ of 100 Å and larger is then explained by a doubling of the Landau level degeneracy, accounting for conduction band states in each individual InAs well. For thin barrier ($t_\mathrm{b} \leq 50\,\text{Å}$) structures, most measurements imply $n_{R_\mathrm{H}} < 2n_\mathrm{SdH}$. The origin of this systematic deviation is not clear. However, an exact agreement between $n_{R_\mathrm{H}}$ and $n_\mathrm{SdH}$ is not expected even for single DHETs as the semiclassical approximation is of limited validity in systems of strongly interacting electrons and holes.

The average electron sheet densities calculated from the experimental data of Table 6.2 are plotted in Fig. 6.10(a) against the barrier thickness $t_\mathrm{b}$. It becomes apparent that the electron concentration increases significantly between $t_\mathrm{b} = 25\,\text{Å}$ and $t_\mathrm{b} = 100\,\text{Å}$ but stays approximately constant for larger barrier thicknesses. The behaviour indicates that for thin barriers the interaction between the wells strongly affects the electron energy levels, whereas the effect is small for $t_\mathrm{b} > 100\,\text{Å}$. The $\mathbf{k}\cdot\hat{\mathbf{p}}$ calculations of Sec. 6.2.3 confirm this picture. In a 2DEG, the density of states is constant and $n_\mathrm{e} = (E_\mathrm{F} - E_0) \times m^*/\hbar^2\pi$. Fig. 6.10(b) shows the bottom of the lowest electron subband $E_0$ relative to the Fermi energy $E_\mathrm{F}$ versus the well distance; the calculation sucessfully reproduces the trend of Fig. 6.10(a). However, the absolute electron densities are overestimated even though the model assumes a significantly lower well width

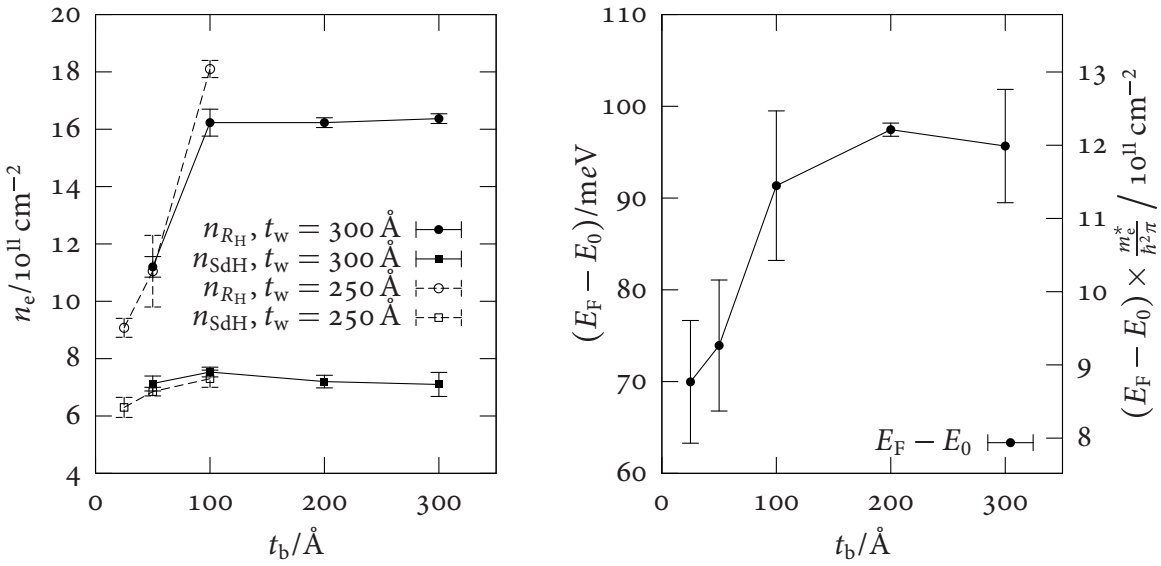


(a) Experimental densities from Table 6.2 (b) Calculated $E_F - E_0$ from Sec. 6.2.3

Figure 6.10: Double well electron density versus spacer thickness.

of 180 Å. The measurements of Table 6.1 also show a weak but consistent decrease in $n_{SdH}$ with decreasing InAs well width; the average absolute values are compatible with the values reported for similar DHETS [4, 12].

As the cap thickness of the samples investigated here is well within the regime for which previous studies have established a negligible influence of the Fermi level pinning at the surface [4], any imbalance between the concentrations of mobile holes and electrons must be a result of charge trapping at the GaSb–InAs interfaces. One therefore expects the samples to show nearly intrinsic behaviour with $n_h \approx n_e$. In this case, the Fermi level lies in the minigap formed by the hybridization between electron and hole states,[4] and the conductivity is suppressed. The semiclassical Drude model then does not describe transport accurately. In a sufficiently high parallel magnetic field, the minigap is removed (*cf.* Sec. 5.5.3); comparing the conductivity in the presence of the field with the zero field value allows to estimate the suppression due to the minigap. In the majority of samples, the conductivity increases by a factor of three or greater once an in-plane magnetic field is applied. The magnitude of the ef-

[4] As the hole band is anisotropic and the position of the minigap depends on the direction, a Fermi contour (surface) none the less exists.

fect is similar to that observed by Lakrimi *et al.* [6,7] in comparable DHETs and superlattices with close to matched electron and hole concentrations.

A closer look at the behaviour at intermediate magnetic fields also exhibits evidence for the presence of a high hole concentration. The Hall resistivity $\rho_{xy}(B_z)$ of all samples shows a series of pronounced local minima which are absent from single carrier systems. In such systems, $\rho_{xy}(B_z)$ shows a step-like monotonic increase with magnetic field. At low enough temperatures, the steps eventually form plateaux with constant resistivity $R_\mathrm{K}/\nu$ extending over the field range where the Fermi energy lies in the gap between two Landau levels; here $R_\mathrm{K} = h/e^2$ and $\nu$ is the (integer) number of occupied Landau levels [15]. This is the famous quantum Hall effect. In electron–hole systems there are separate Landau fans for electrons and holes and the quantized Hall resistivity is $\rho_{xy} = R_\mathrm{K}/(\nu_\mathrm{e} - \nu_\mathrm{h})$. If the two Landau fans overlap, as they can do in GaSb–InAs heterostructures owing to the crossed band alignment at the interface, the Fermi energy will oscillate between electron and hole levels and $\rho_{xy}(B_z)$ no longer increases monotonically [2,16,17]. The minima in the observed Hall resistivity are the remnants of this compensated quantum Hall effect after Landau level broadening.

### 6.4.2 Interaction

The correspondence between the Hall resistivity features in the respective traces in Fig. 6.3(b) suggests that both the position of the Fermi level and the Landau level structure are similar for the samples with 300 nm, 200 nm and 100 nm GaSb barrier thickness. One can therefore assume that in this range the interaction between the individual wells is small, an idea that is further supported by the similarity to the single well data.

The smaller barrier results show less consistency; while I cannot entirely dismiss the possibility that the differences are a result of varying sample quality caused by changes in the MOVPE growth conditions, an explanation based on the increased interaction between the individual carrier sheets is plausible. Looking back to the preliminary calculations of Sec. 6.2.3, there are several ways in which the energy spectrum might be affected: a reduction of the

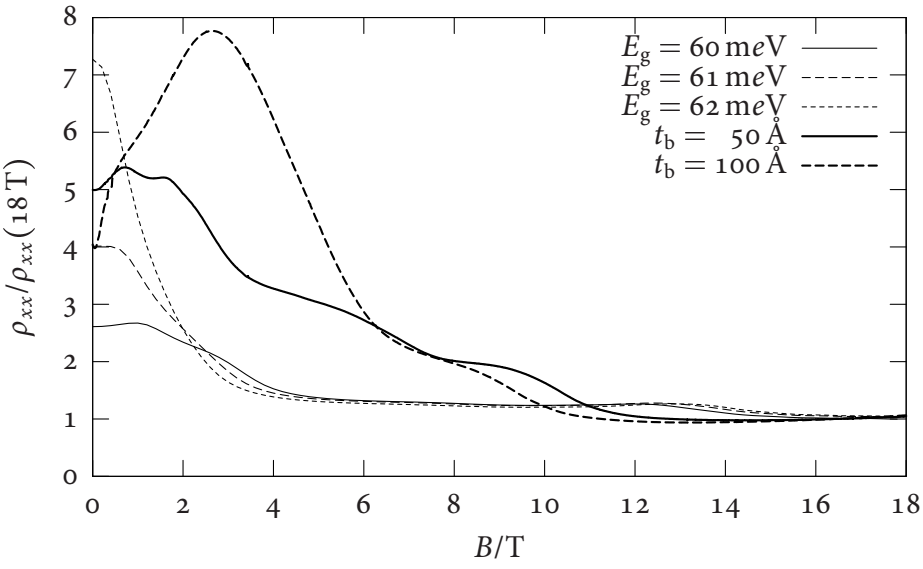


Figure 6.11: Comparison of parallel field magnetoresistivity with theory. The experimental data (thick) are taken from Fig. 6.7(a); the calculated curves assume $\Delta = 7\,meV$, $E_F = 54\,meV$, and $\delta z = 180\,Å$. The resistivity is given in terms of the resistivity at high field.

energy difference between occupied electron and hole subbands; hybridization between conduction band states in different wells; and the appearance of distinct hole states in the barrier that are no longer degenerate with hole states in the cap or buffer layer. The latter effect in particular would lead to a more complex level structure and affect the magnetic field dependence of the resistivity tensor. However, as there is still considerable broadening in the experimental data even at 0·5 K and a realistic model that correctly predicts confinement energies is still missing, a detailed test of these ideas is presently not possible.

The two-band model of Sec. 5.5.3 partially explains the basic features of most parallel field magnetoresistance measurements. Fig. 6.11 compares the experimental data of Fig. 6.7(a) to the prediction calculated from Eq. (5.18) for $E_F - E_0 = 54\,meV$, corresponding to $n_e \approx 6{\cdot}8 \times 10^{11}\,cm^{-2}$, $\delta z = 180\,Å$ and taking $\Delta = 7\,meV$ [6,18]. As explained in Sec. 5.5.3, the two prominent features correspond to parallel field values at which anticrossing occurs at the Fermi energy, *i.e.*, the sides of the (hypothetical non-interacting) hole Fermi contour pass the electron Fermi circle. For realistic values of $E_F$, $\Delta$, and $\delta z$, the quantitative agreement is poor

and the model does not predict either a strong second maximum or a magnetoresistance that does not saturate at parallel fields up to 18 T. Similar pronounced double peak structures have previously appeared in superlattice measurements [7]. In both superlattices and the present double well structures, more than two carrier gases are present, and further hybridization gaps, which are not accounted for in the simplistic model, can form. Effects of the in-plane field other than the relative shift of the dispersion relations are also ignored; in particular, the scattering time $\tau$ is assumed to be independent of $B_\parallel$.

### 6.4.3 Symmetry

The double well structures are nominally symmetrical about the GaSb barrier, and the electron states in both InAs wells as well as the hole states in the GaSb buffer and cap layers should be equivalent. In reality, this symmetry can be broken by the Fermi level pinning at the free GaSb surface or by trapped charges at the GaSb–InAs interfaces. In fact, the electronic properties of single well DHETs grown under similar conditions are best explained by models containing only two conduction channels representing electrons in the InAs well and holes in the GaSb buffer, with no hole occupancy in the GaSb cap [4, 12].

As reasoned in Sec. 6.4.1, both wells contribute to the overall conductivity with individual electron densities similar to those of comparable DHETs. Parallel conduction through two independent electronic channels with slightly different sheet concentrations would lead to an interference between the Shubnikov–de Haas-oscillations corresponding to each channel and the emergence of a beating pattern. The oscillations of Fig. 6.6 exhibit only a single dominating frequency and no indication of beating. By taking the inverse field range over which oscillations are observable (around $1\,\mathrm{T}^{-1}$) as the minimum distance between nodes of the envelope function, one estimates an conservative upper limit on the difference between the carrier concentrations of $5 \times 10^{10}\,\mathrm{cm}^{-2}$. This translates to a maximal difference in the position of the Fermi level relative to the bottom of the conduction band of approximately 5 m$e$V across the entire double well structure. A comparison between the behaviour of the

two wells is not sensitive to an asymmetry between the top and bottom interfaces of each individual InAs layer, and the present analysis cannot address this question.

## 6.5 Conclusions

I have investigated a range of samples containing two adjacent InAs wells using only magnetoresistance measurements at moderately low temperatures from 0·5 to 4·2 K and high fields up to 18 T. The samples were designed with thick cap layers of at least 1500 Å to minimize the effect of surface states and there is considerable evidence that most samples are nearly intrinsic. However, the low mobility of the hole gas and the hybridization between InAs conduction band states and GaSb valence band states prevent an accurate determination of the hole concentration.

For distances between the wells of 100 Å and above, the structures behave essentially like two DHETs conducting in parallel. Within the accuracy of the measurements, the wells behave identically, putting an upper limit of at most 5 meV on the variation of the Fermi level relative to the bottom of the conduction band throughout the double well system. At smaller well distances, qualitatively different behaviour is observed. Based on model calculations, which, however, do not accurately reflect the energy spectrum of actual samples, it is suggested that the change in hole energy levels in the GaSb barrier and the resulting change in charge distribution become important in this regime.

The magnetoresistance in a magnetic field in the plane of the InAs wells shows large and unsystematic changes between different samples and even between different parts of the same structure. The results have been discussed in the light of the two band hybridization model introduced in the previous Chapter. The theoretical model predicts a strong dependence on the position of the Fermi energy and the band overlap, which likely plays a part in the observed variation. Individual features attributed to the crossing of the electron and hole Fermi contours, which are also seen in DHETs, can be recognized in the double well data, but the quantitative agreement between theory and experiment is poor. In particular, the rel-

ative height of the peaks around 10 T that are seen in many experimental traces cannot be explained in a simple two-band model.

## Bibliography

[1] D. M. Symons, M. Lakrimi, R. J. Nicholas, D. K. Maude, J. C. Portal, N. J. Mason, and P. J. Walker. Magnetic breakdown in the semimetallic InAs/GaSb system. *Physical Review B*, 58(11):7292–7299, September 1998.

[2] R. J. Nicholas, K. Takashina, M. Lakrimi, B. Kardynał, S. Khym, and N. J. Mason. Metal-insulator oscillations in a two-dimensional electron-hole system. *Physical Review Letters*, 85(11):2364–2367, September 2000.

[3] R. J. Nicholas, M. Lakrimi, B. Kardynał, S. Khym, N. J. Mason, J. Rehman, K. Takashina, P. J. Walker, D. M. Symons, D. K. Maude, and J. C. Portal. A digital quantum Hall effect. *Physica E*, 6:836–839, 2000.

[4] K. Takashina. *Magneto-transport Studies of GaSb/InAs/GaSb Double-heterostructures*. DPhil thesis, University College, University of Oxford, 2002.

[5] M. S. Daly, K. S. H. Dalton, M. Lakrimi, N. J. Mason, R. J. Nicholas, M. van der Burgt, P. J. Walker, D. K. Maude, and J. C. Portal. Zero-Hall-resistance state in a semimetallic InAs/GaSb superlattice. *Physical Review B*, 53(16):10524–10527, April 1996.

[6] M. Lakrimi, S. Khym, R. J. Nicholas, D. M. Symons, F. M. Peeters, N. J. Mason, and P. J. Walker. Minigaps and novel giant negative magnetoresistance in InAs/GaSb semimetallic superlattices. *Physical Review Letters*, 79(16):3034–3037, October 1997.

[7] M. Lakrimi, S. Khym, D. M. Symons, R. J. Nicholas, F. M. Peeters, N. J. Mason, and P. J. Walker. Mini-gaps and novel giant negative magnetoresistance in InAs/GaSb semimetallic superlattices. *Physica E*, 2:363–367, 1998.

[8] A. J. L. Poulter, M. Lakrimi, R. J. Nicholas, N. J. Mason, and P. J. Walker. Optical probing of the minigap in InAs/GaSb semimetallic superlattices. *Physica B*, 256–258:256–259, 1998.

[9] J. M. Luttinger and W. Kohn. Motion of electrons and holes in perturbed period fields. *Physical Review*, 97(4):869–883, February 1955.

[10] J. M. Luttinger. Quantum theory of cyclotron resonance in semiconductors: General theory. *Physical Review*, 102(4):1030–1041, May 1956.

[11] T. A. Vaughan. *Magneto-optics of InAs/GaSb Heterostructures*. DPhil thesis, Brasenose College, University of Oxford, 1995.

[12] C. Petchsingh. *Cyclotron Resonance Studies on InAs/GaSb Heterostructures*. DPhil thesis, Wolfson College, University of Oxford, 2002.

[13] P.-O. Löwdin. On the non-orthogonality problem connected with the use of atomic wave functions in the theory of molecules and crystal. *Journal of Chemical Physics*, 18(3):365–375, March 1950.

[14] E. O. Kane. Band structure of indium antimonide. *Journal of Physics and Chemistry of Solids*, 1(4):249–261, January 1957.

[15] K. von Klitzing, G. Dorda, and M. Pepper. New method for high-accuracy determination of the fine-structure constant based on quantized Hall resistance. *Physical Review Letters*, 45(6):494–497, August 1980.

[16] E. E. Mendez, L. Esaki, and L. L. Chang. Quantum Hall effect in a two-dimensional electron-hole gas. *Physical Review Letters*, 55(20):2216–2219, November 1985.

[17] M. S. Daly, D. M. Symons, M. Lakrimi, R. J. Nicholas, N. J. Mason, and P. J. Walker. Interface composition dependence of the band offset in InAs/GaSb. *Surface Science*, 361/362:205–208, 1996.

[18] J.-C. Chiang, S.-F. Tsay, Z. M. Chau, and I. Lo. Conduction-valence Landau level mixing effect. *Physical Review Letters*, 77(10):2053–2056, September 1996.